



Cite as  
Nano-Micro Lett.  
(2022) 14:215

Received: 11 September 2022  
Accepted: 18 October 2022  
Published online: 7 November 2022  
© The Author(s) 2022

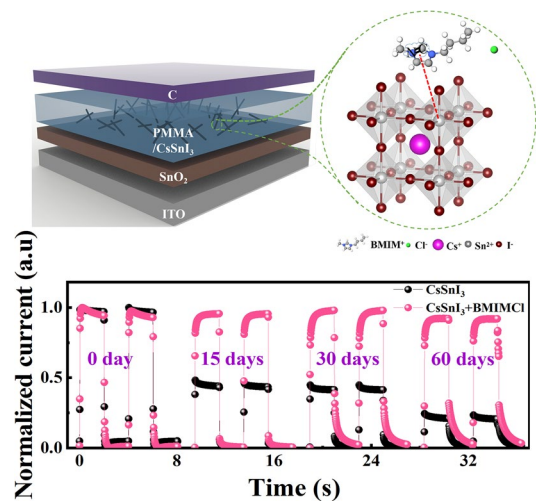
# Defect Passivation on Lead-Free CsSnI<sub>3</sub> Perovskite Nanowires Enables High-Performance Photodetectors with Ultra-High Stability

Zheng Gao<sup>1,2,3</sup>, Hai Zhou<sup>1</sup> ✉, Kailian Dong<sup>2</sup>, Chen Wang<sup>2</sup>, Jiayun Wei<sup>3</sup>, Zhe Li<sup>2</sup>, Jiashuai Li<sup>2</sup>, Yongjie Liu<sup>2</sup>, Jiang Zhao<sup>3</sup> ✉, Guojia Fang<sup>2</sup> ✉

## HIGHLIGHTS

- Through materials analysis and theoretical calculations, the defects of CsSnI<sub>3</sub> nanowires (NWs) were effectively passivated via incorporating 1-butyl-2,3-dimethylimidazolium chloride into perovskites.
- The high-performance CsSnI<sub>3</sub> NW photodetectors (PDs) were achieved with a responsivity of up to 0.237 A W<sup>-1</sup>, a high detectivity of 1.18 × 10<sup>12</sup> Jones and a linear dynamic range of 180 dB. These values are comparable to the reported high-performance Pb-based perovskite PDs and higher than those of the Pb-free perovskite PDs.
- Our unpackaged devices exhibit ultra-high stability with no degradation after 60 days of storage in air (25 °C, 50% humidity).

**ABSTRACT** In recent years, Pb-free CsSnI<sub>3</sub> perovskite materials with excellent photoelectric properties as well as low toxicity are attracting much attention in photoelectric devices. However, deep level defects in CsSnI<sub>3</sub>, such as high density of tin vacancies, structural deformation of SnI<sub>6</sub><sup>-</sup> octahedra and oxidation of Sn<sup>2+</sup> states, are the major challenge to achieve high-performance CsSnI<sub>3</sub>-based photoelectric devices with good stability. In this work, defect passivation method is adopted to solve the above issues, and the ultra-stable and high-performance CsSnI<sub>3</sub> nanowires (NWs) photodetectors (PDs) are fabricated via incorporating 1-butyl-2,3-dimethylimidazolium chloride salt (BMIMCl) into perovskites. Through materials analysis and theoretical calculations, BMIM<sup>+</sup> ions can effectively passivate the Sn-related defects and reduce the dark current of CsSnI<sub>3</sub> NW PDs. To further reduce the dark current of the devices, the polymethyl methacrylate is introduced, and finally, the dual passivated CsSnI<sub>3</sub> NWPDs show ultra-high performance with an ultra-low dark current of 2 × 10<sup>-11</sup> A, a responsivity of up to 0.237 A W<sup>-1</sup>, a high detectivity of 1.18 × 10<sup>12</sup> Jones and a linear dynamic range of 180 dB. Furthermore, the unpackaged devices exhibit ultra-high stability in device performance after 60 days of storage in air (25 °C, 50% humidity), with the device performance remaining above 90%.



**KEYWORDS** Pb-free; Perovskite; CsSnI<sub>3</sub>; Photodetector; Nanowire

✉ Hai Zhou, [hizhou@dgut.edu.cn](mailto:hizhou@dgut.edu.cn); Jiang Zhao, [zhaojiang@hubu.edu.cn](mailto:zhaojiang@hubu.edu.cn); Guojia Fang, [gjfang@whu.edu.cn](mailto:gjfang@whu.edu.cn)

<sup>1</sup> International School of Microelectronics, Dongguan University of Technology, Dongguan 523808, Guangdong, People's Republic of China

<sup>2</sup> Key Lab of Artificial Micro- and Nano-Structures of Ministry of Education of China, School of Physics and Technology, Wuhan University, Wuhan 430072, People's Republic of China

<sup>3</sup> Faculty of Physics and Electronic Science, Hubei University, Wuhan 430062, People's Republic of China



## 1 Introduction

Because of excellent photoelectronic properties and low fabrication cost, organic–inorganic hybrid perovskites have become a hot topic in recent years and are widely used in solar cells [1–4], photodetectors (PDs) [5–7], light-emitting diodes (LEDs) [8, 9], etc. Until now, the highest certified power conversion efficiency of perovskite solar cells has exceeded 25% [10, 12], and the LEDs based on lead-containing perovskite materials also show high performance; for example, the highest external quantum efficiency of green LEDs has exceeded 20% [13–15]. However, the presence of heavy metal lead severely limits the commercialization of lead halide materials, which will face security risks of heavy metal lead leakage during mass production, transportation, installation and operation.

In this context, lead-free perovskite materials based on tin (Sn) [14], bismuth [15], germanium [16], antimony [17] or copper [18] have attracted much attention. Among these lead-free perovskite materials, CsSnI<sub>3</sub> is more popular in photovoltaic applications due to its similar crystal and electronic structure to its Pb-based counterpart. Besides, inorganic perovskite CsSnI<sub>3</sub> has a narrow optical band gap close to the Shockley–Queisser limit, with long lifetime and high charge carrier mobility [19, 20]. Moreover, the melting point of the CsSnI<sub>3</sub> is up to 451 °C, which means that it has excellent inherent thermal stability. Therefore, the development of the inorganic perovskite CsSnI<sub>3</sub> shows great prospect, and many scientists have achieved meaningful results [21–23]. Jin et al. [24] reported the growth of CsSnX<sub>3</sub> (X = Br, I) perovskite semiconductors with controlled orientation and size by high-temperature vapor-phase epitaxy on mica sheets. Yang et al. [25] reported the preparation of CsSnX<sub>3</sub> (X = Cl, Br, and I) perovskite nanowire (NW) arrays by chemical vapor deposition with a responsivity of 54 mA W<sup>-1</sup>, a detectivity of 3.85 × 10<sup>-5</sup> Jones, and fast rise and decay time constants of 83.8 and 243.4 ms, respectively. However, the efficiency of the solution-processed CsSnI<sub>3</sub> devices was much lower than that of the Pb-based analogs, mainly due to the weak Sn–I bond of inorganic CsSnI<sub>3</sub>, which causes lower tin vacancy formation energy and the easy oxidation of Sn<sup>2+</sup> to Sn<sup>4+</sup>, leading to a high level of self-P doping in inorganic CsSnI<sub>3</sub> perovskites, and the reduction in the device performance and the decrease in the output stability [26]. Therefore, strategies to passivate the Sn defects in inorganic

CsSnI<sub>3</sub> perovskites while maintaining their environmental stability are urgently needed.

In this work, 1-butyl-2,3-dimethylimidazolium chloride (BMIMCl) salt is introduced to passivate the defects of perovskite CsSnI<sub>3</sub> NWs. Through materials analysis and theoretical calculations, the BMIMCl has a strong passivating effect on Sn-related defects via large  $\pi$ -bonds in N–C=N, and the lone pair of electrons in large  $\pi$ -bonds enhances the electron density around Sn<sup>2+</sup> in CsSnI<sub>3</sub> and protects it from oxidation to Sn<sup>4+</sup>; thus, the fabricated CsSnI<sub>3</sub> NWs with BMIMCl show high light absorption, low defect density and air stability. To further reduce the dark current of the devices, the polymethyl methacrylate (PMMA) was applied, and finally, the dual passivated CsSnI<sub>3</sub> NW PDs show ultra-high performance with an ultra-low dark current of 2 × 10<sup>-11</sup> A, a high responsivity of 0.237 A W<sup>-1</sup>, a high detectivity of 1.18 × 10<sup>12</sup> Jones and a linear dynamic range (LDR) of 180 dB. Besides, our unpackaged devices exhibit good stability with less than 10% degradation in device performance after 60 days of storage in air (25 °C, 50% humidity), demonstrating good application potential.

## 2 Experimental and Calculation

### 2.1 Device Fabrication

A pre-etched indium-tin oxide (ITO) glass substrate was ultrasonically cleaned with detergent, deionized water, ethanol and iso-propyl alcohol for 15 min, respectively. To prepare the SnO<sub>2</sub> precursor solution, the SnO<sub>2</sub> stock solution (1 mL) was diluted in deionized water (4 mL). The as-cleaned ITO substrate was treated with UV ozone at 100 °C for 10 min. A compact layer of SnO<sub>2</sub> was spin-coated on top of the ITO at 4000 rpm for 30 s. Then, it was heated at 150 °C for 30 min in air. After that, the samples were treated with UV ozone for 10 min. Subsequently, the samples were transferred into a N<sub>2</sub> filled glovebox with H<sub>2</sub>O and O<sub>2</sub> concentrations of < 0.1 ppm. A layer of PbI<sub>2</sub> film was fabricated by spin-coating PbI<sub>2</sub>/BMIMCl (1 mol mL<sup>-1</sup>/0, 5, 8, 10 and 15 mg mL<sup>-1</sup>) in DMF at 3000 rpm for 30 s, followed by annealing at 70 °C for 10 min. Then, the substrate was soaked in the prepared CsI/SnI<sub>2</sub>/SnF<sub>2</sub> (5 /4 /0.4 mg mL<sup>-1</sup>) solution in anhydrous methanol for 2 h. After that, the substrates were placed in an isopropyl alcohol solution for 20 s and then annealed at 180 °C for 10 min. Finally, a layer of

PMMA was coated on the samples by spin-coating PMMA in CB ( $20 \text{ mg mL}^{-1}$ ) at 2000/3000/4000/5000/6000/7000 rpm for 30 s, followed by annealing at  $100 \text{ }^\circ\text{C}$  for 10 min. Then, a layer of carbon electrode was scraped on the samples and annealed at  $120 \text{ }^\circ\text{C}$  for 15 min in air.

## 2.2 Calculations

All the calculations are performed in the framework of the density functional theory (DFT) with the projector augmented plane-wave method, as implemented in the Vienna ab initio simulation package. The generalized gradient approximation proposed by Perdew, Burke and Ernzerhof is selected for the exchange–correlation potential. The long-range van der Waals interaction is described by the DFT-D3 approach. The cutoff energy for plane wave is set to 400 eV. The energy criterion is set to  $10^{-5}$  eV in iterative solution of the Kohn–Sham equation. The Brillouin zone integration is performed at the Gamma point for structural optimization, and a  $3 \times 3 \times 1$  k-mesh grid is used for electronic structure calculations. All the structures are relaxed until the residual forces on the atoms have declined to less than  $0.05 \text{ eV } \text{Å}^{-1}$ .

## 3 Results and Discussion

A schematic diagram of the preparation of  $\text{CsSnI}_3$  NWs by a two-step solution method is shown in Fig. 1a. The aqueous  $\text{SnO}_2$  solution was first spin-coated onto a clean ITO substrate and then annealed on a hot table at  $150 \text{ }^\circ\text{C}$  for 30 min to obtain the  $\text{SnO}_2$  films. The  $\text{PbI}_2/\text{BMIMCl}$  ( $1 \text{ mol mL}^{-1}/0, 5, 8, 10$  and  $15 \text{ mg mL}^{-1}$ ) DMF solution was spin-coated on the  $\text{SnO}_2/\text{ITO}$  substrate and then annealed at  $70 \text{ }^\circ\text{C}$  for 10 min to obtain the  $\text{PbI}_2\text{-BMIMCl}$  films. The  $\text{PbI}_2\text{-BMIMCl}$  film-covered substrates were immersed in a methanol solution of  $\text{CsI}/\text{SnI}_2/\text{SnF}_2$  ( $5/4/0.4 \text{ mg mL}^{-1}$ ) for 2 h. The yellow phase  $\text{CsSnI}_3$  ( $\gamma\text{-CsSnI}_3$ ) was obtained by the B-position exchange reaction. During the reaction, the perovskite also grows in a specific direction because of the strong anisotropy of  $\gamma\text{-CsSnI}_3$  and eventually forms one-dimensional  $\gamma\text{-CsSnI}_3$  NWs [27, 28]. After that, the  $\text{CsSnI}_3$  NWs-covered substrates were placed in an isopropyl alcohol solution for 20 s to wash away the impurities on it and then annealed at  $180 \text{ }^\circ\text{C}$  for 10 min to obtain the black phase  $\text{CsSnI}_3$  NWs (B- $\text{CsSnI}_3$  NWs). The top-view scanning electron microscopy (SEM) images of  $\text{CsSnI}_3$  NW films with

different soaking times (2, 4, 8, 16, 24, and 48 h) are shown in Figs. 1b and S1, which show little changes in surface morphology. Besides, the energy-dispersive spectroscopy (EDS) results (Table S1) show that when the soaking time is above 2 h, the perovskite NWs indicate very little Pb content ( $\sim 0.21\%$ ) and we think our perovskite nanowires are basically all converted to  $\text{CsSnI}_3$  NWs and 2 h of soaking time are enough.

When different BMIMCl concentrations (5, 8, 10 and  $15 \text{ mg mL}^{-1}$ ) are incorporated (Fig. S2), the surface coverage of the nanowires is more obvious with the increase in the concentration. In order to further study the effect of the incorporation of BMIMCl, the high-resolution transmission electron microscopy (HRTEM) is performed, and the results are shown in Figs. 1c and S4. From these figures, all perovskite NW samples show high crystallinity. The d-spacing value of the  $\text{CsSnI}_3$  without BMIMCl is estimated to be 0.31 nm, corresponding to the (202) plane of  $\text{CsSnI}_3$ . For the BMIMCl +  $\text{CsSnI}_3$  sample, the spacing between the lattice fringe is 0.35 nm, which corresponds to the (220) plane of  $\text{CsSnI}_3$ , and shows clearer lattice fringes of the perovskite grains, indicating higher crystallinity of the perovskite grains [29, 30]. Besides, the NW is covered by an amorphous BMIMCl molecular layer with a thickness of about 1.2 nm. This thin layer of BMIMCl will protect the underlying  $\text{CsSnI}_3$  from degradation when exposed to ambient air.

Figures 1d and S3a show the X-ray diffraction (XRD) patterns of  $\text{CsSnI}_3$  NW films with different concentrations of BMIMCl, which match well with the orthorhombic perovskite crystal structure. After the addition of BMIMCl, the peak intensity of the (220) plane of the  $\text{CsSnI}_3$  NW film is slightly enhanced compared with that of the unincorporated  $\text{CsSnI}_3$  NW film, the better crystal quality of the perovskite may improve the carrier transmission of the  $\text{CsSnI}_3$  [31]. Figures 1e and S3b show the optical properties of the perovskite with different concentrations of BMIMCl, which show the  $\text{CsSnI}_3$  NWs have capacity of absorbing from visible to infrared light. Steady-state photoluminescence (PL) spectroscopy is then performed to examine the emission characteristics of the  $\text{CsSnI}_3$  NW thin films (Figs. 1f and S3c). Compared with the  $\text{CsSnI}_3$  NW film without BMIMCl, the peak intensity of the  $\text{CsSnI}_3$  NW film gradually increases with increasing the concentration of BMIMCl and reaches a maximum at the concentration of  $8 \text{ mg mL}^{-1}$ . Then, the peak intensity gradually decreases after further increasing the concentration of BMIMCl. This can be explained that

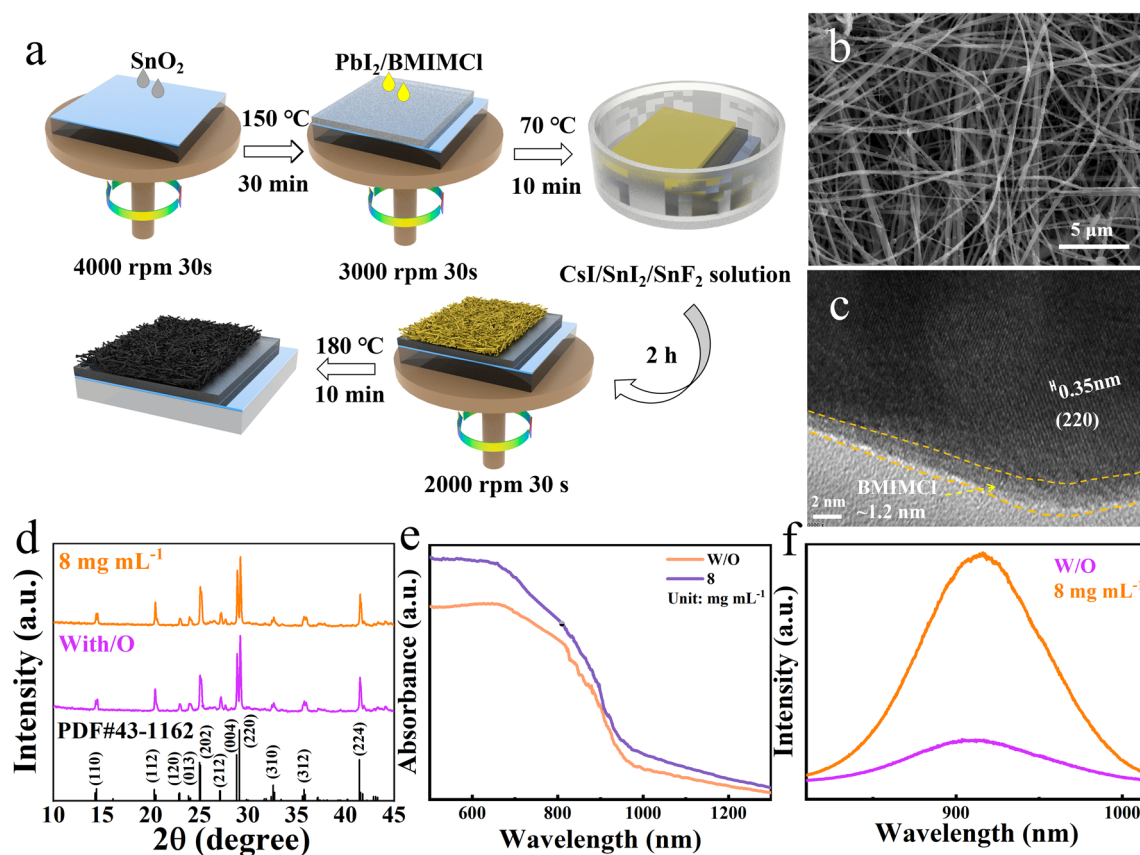


**Fig. 1** **a** Flow chart for the preparation of CsSnI<sub>3</sub> NWs. **b** Surface SEM and **c** HRTEM of CsSnI<sub>3</sub> NWs with BMIMCl. **d** XRD, **e** optical absorption and **f** steady-state PL curves of CsSnI<sub>3</sub> NWs with or without 8 mg mL<sup>-1</sup> BMIMCl

the moderate BMIMCl concentration can effectively passivate the defects of the CsSnI<sub>3</sub> NWs and suppress the non-radiative recombination of the perovskites [23, 32]. Besides, the time-resolved PL indicates that the CsSnI<sub>3</sub> NW film with 8 mg mL<sup>-1</sup> BMIMCl shows longest carrier lifetime (Fig. S4d), which further confirms moderate BMIMCl concentration is beneficial for passivating the defects of the CsSnI<sub>3</sub> NWs.

Figure 2a shows the CsSnI<sub>3</sub> NWPD with an ITO/SnO<sub>2</sub>/perovskite NWs/carbon structure, in which SnO<sub>2</sub> is used as the electron transport layer, perovskite NWs are the photoactive layer, and carbon is as the top electrode also protects perovskites from corrosion by water and oxygen in air. As a high-performance PD, low dark current is essential, which has a positive impact on the linear dynamic range, signal-to-noise ratio and detectivity of the device. The relationship between the light and dark current of the PDs is shown in Fig. 2b, and 8 devices are used for the light/dark current statistic. The dark current gradually decreases as the BMIMCl

concentration increases, and the dark current reaches a minimum until the concentration is at 8 mg mL<sup>-1</sup>. The drop in dark current is attributed to the passivation of the surface defects of perovskite, especially the Sn vacancies, which are the main culprit for the material to appear metallic [21]. However, too much ionic liquid will cause additional impurities, which will increase the dark current of the device. For the photocurrent, it shows a slightly downward trend. Considering the light and dark currents comprehensively, we believe that the NWPDs prepared at 8 mg mL<sup>-1</sup> are best.

To investigate the passivation interaction of the BMIMCl on Sn-related defects and verify our conjecture, Fourier transform infrared spectroscopy (FTIR) measurements are performed on BMIMCl and BMIMCl + CsSnI<sub>3</sub>. The peak of the pure BMIMCl sample is located at 1589 cm<sup>-1</sup> (Fig. 3a), which corresponds to the N–C=N stretching vibration of the imidazole ring. For the BMIMCl + CsSnI<sub>3</sub> sample, this peak is red-shifted to 1584 cm<sup>-1</sup>, indicating a strong interaction between N–C=N and CsSnI<sub>3</sub>. It is inferred that the

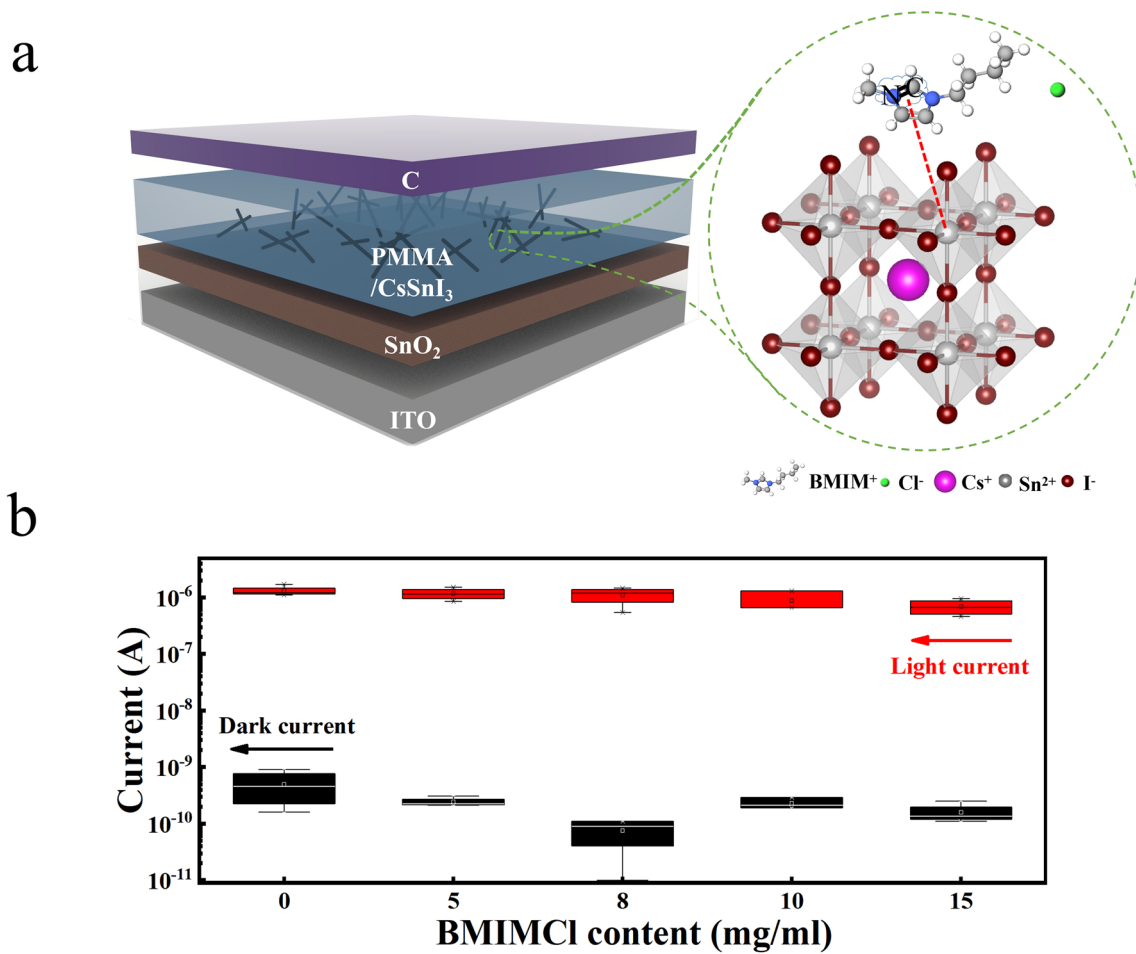


**Fig. 2** a Schematic structure of a PD based on the CsSnI<sub>3</sub> with BMIMCl. b Device light/dark current statistic data under the addition of different levels of BMIMCl

N–C = N of BMIM<sup>+</sup> has a strong passivating interaction with Sn-related defects such as Sn vacancies. The trap density of the Sn-based perovskites is strongly associated with the Sn<sup>4+</sup> content, which is considered as the Sn vacancies and can be distinguished by X-ray photoelectron spectroscopy (XPS) measurement. As shown in Fig. 3b, compared with ordinary CsSnI<sub>3</sub> samples, the proportion of Sn<sup>4+</sup> in the BMIMCl + CsSnI<sub>3</sub> sample is greatly reduced, and the proportion of Sn<sup>2+</sup> rises, which indicates that the oxidation of Sn<sup>2+</sup> to Sn<sup>4+</sup> in the BMIMCl + CsSnI<sub>3</sub> sample is significantly suppressed. In order to further verify our conjecture, the DFT calculations are used to study the effect of the introduction of BMIMCl on CsSnI<sub>3</sub>. Since the BMIMCl is coated on the surface of CsSnI<sub>3</sub> perovskite, a model of BMIMCl on CsSnI<sub>3</sub> is established, and the calculated differential charge density of BMIMCl + CsSnI<sub>3</sub> (220) indicates the effective

charge extraction of BMIMCl, as shown in Fig. 3c. Besides, the density of state (DOS) of CsSnI<sub>3</sub> perovskites with or without BMIMCl is calculated, as shown in Fig. 3d. It can be clearly observed that compared with CsSnI<sub>3</sub>, the DOS of CsSnI<sub>3</sub> after BMIMCl passivation is significantly reduced in electron defects near the Fermi level, indicating the reduction in charge carrier recombination in CsSnI<sub>3</sub> after BMIMCl passivation and the promotion of electron transport in the perovskite.

Previous reports showed that the PMMA can fill the voids of the nanowires, passivate the surface defects of the perovskites [33] and can also generate Fowler–Nordheim tunneling to enhance device performance [34]. Based on these, we further adopt the PMMA to reduce the dark current and enhance the device performance. Through optimize the rotational speed, the appropriate thickness of the PMMA

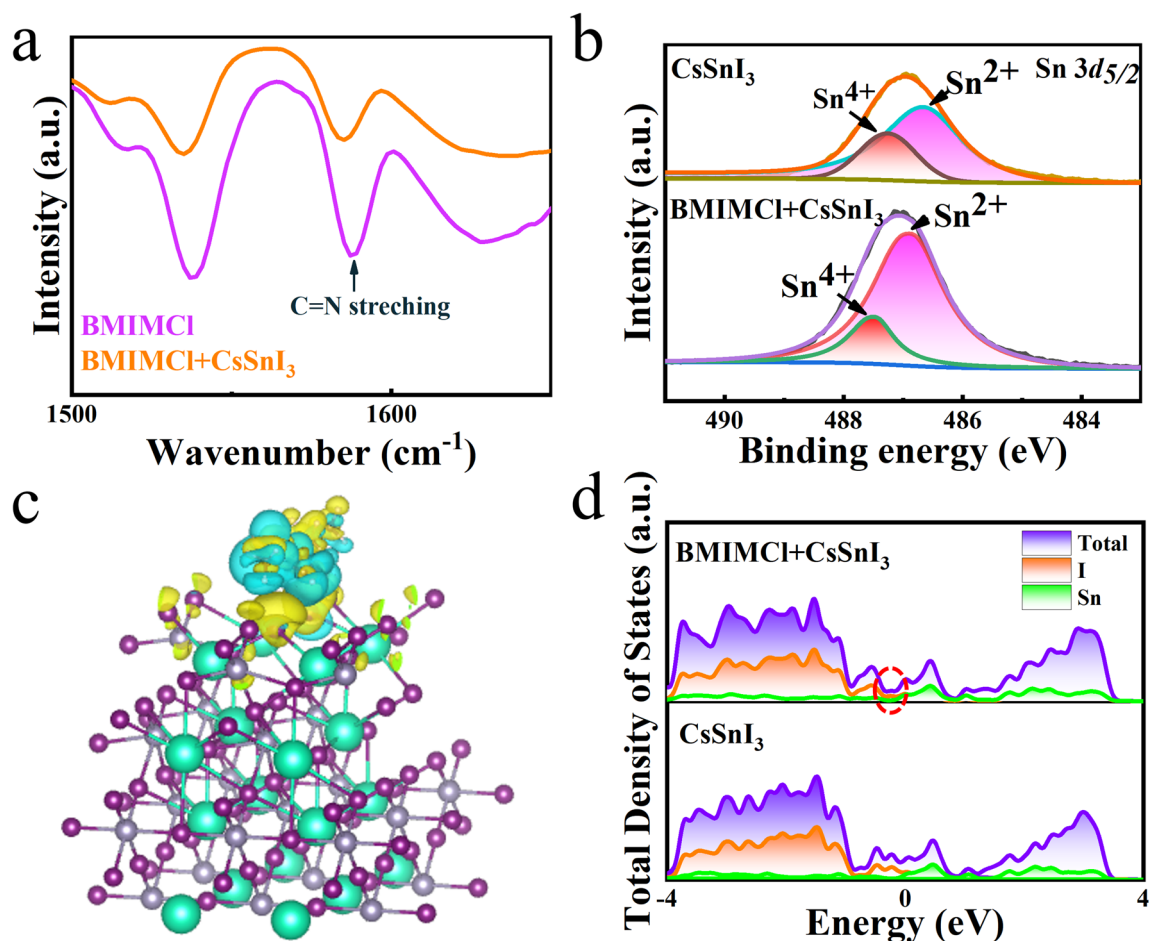


**Fig. 3** **a** FTIR spectra of the BMIMCl and CsSnI<sub>3</sub> with BMIMCl at the wavenumber of 1500–1650 cm<sup>-1</sup>. **b** XPS spectra of Sn 3d of the CsSnI<sub>3</sub> without and with BMIMCl. **c** Differential charge density of the BMIMCl on CsSnI<sub>3</sub>. **d** Total density of state of the perovskite and the BMIMCl passivated perovskite

is obtained at 5000 rpm (Fig. S5a), and at this rotational speed, the device filled by the PMMA shows the lowest dark current and the biggest light current.

The detailed device performances are shown in Fig. 4. As shown in Fig. 4a, under the irradiation of 405 nm laser with different illumination intensities, our device exhibits good photoresponse characteristics to both strong and weak light. From this figure, there is a three-order-of-magnitude difference in dark current under different light intensities. We think the main reason of the three-order-of-magnitude increase in dark current is attributed to the perovskite CsSnI<sub>3</sub>, in which a few Sn vacancies still exist. When the device is illuminated by light, a large number of photo-generated carriers will be generated, and some of them may be trapped by these vacancies and remain. After the light

is removed, these remaining photo-generated carriers will be slowly released and cause the rise of the dark current. When stronger light is applied, more photo-generated carriers are generated and more left, resulting in a three-order of magnitude difference in dark current under different light intensities.

The LDR of the PD is an important parameter for evaluating the performance of the PD, which can be calculated by the formula:

$$\text{LDR} = 20 \log \frac{P_{\text{sat}}}{P_{\text{low}}} \quad (1)$$

where  $P_{\text{sat}}$  and  $P_{\text{low}}$  are the strongest and weakest light intensities, respectively, when the incident light begins to deviate from the linear photocurrent. The calculated LDR is as high as 180 dB, indicating that our device can work stably in a

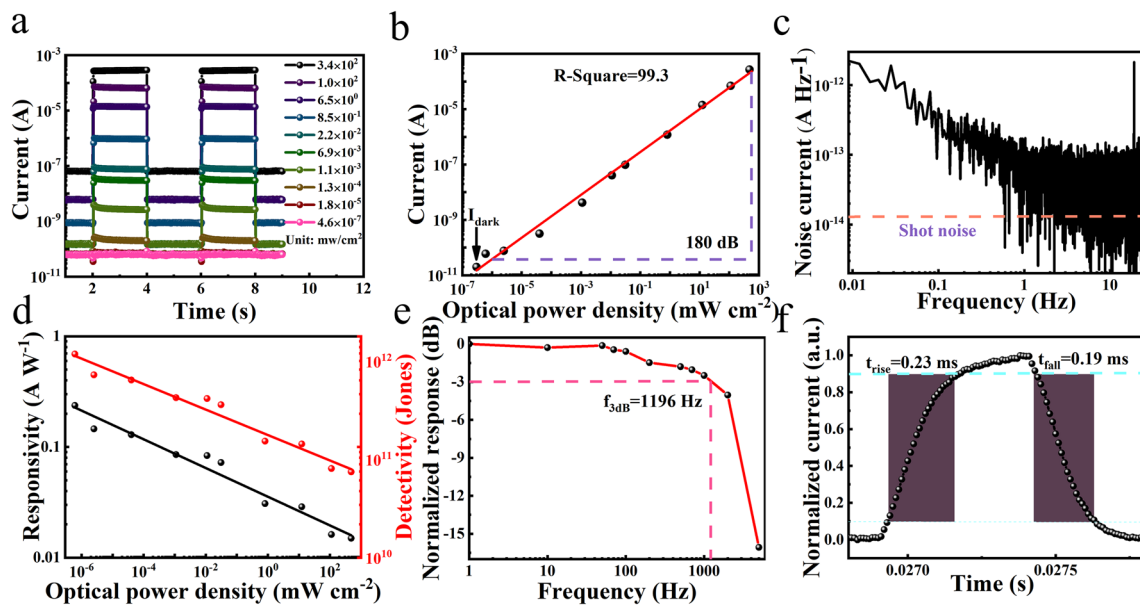


**Fig. 4** Device performances of the dual passivated PDs: **a** current–time curves at different light intensities; **b** LDR; **c** noise current curve; **d** responsivity and detectability *versus* light intensity curves; **e**  $f_{-3\text{dB}}$  bandwidth; **f** response/recovery time. All curves are measured at 0 V

wide range of the light intensity (Fig. 4b), and the ultra-low dark current of  $2 \times 10^{-11}$  A of the device is obtained. Besides, the noise of the device affects the sensitivity of the PD to light, and shot noise is an important noise source which affects the dark current. The device noise power spectrum (Fig. 4c) shows that the noise ( $i_n$ ) of the CsSnI<sub>3</sub> NW PD is very low with the value of about  $4 \times 10^{-13}$  A Hz<sup>-1</sup>. Through the dark current, the shot noise of the device is further calculated, and it is close to the total noise, indicating that the main device noise is the shot noise. To further study the performance of the device, the responsivity  $R$  and the detectivity  $D^*$  are measured to evaluate the sensitivity of the photoelectric response of the device to incident light, which are calculated by the formulas:

$$R = \frac{I_{ph}}{AP_{opt}} \tag{2}$$

$$D^* = \frac{R\sqrt{AB}}{i_n} \tag{3}$$

where  $I_{ph}$  is the photocurrent,  $A$  is the effective light irradiation area of the PD,  $P_{opt}$  is the light intensity, and  $B$  is the detection line width. As shown in Fig. 4d, both the  $R$  and the  $D^*$  show a linear drop with increasing the light intensity. Under weak light, our PD shows high device performance with a  $R$  of 0.237 A W<sup>-1</sup>, and a  $D^*$  of up to  $1.18 \times 10^{12}$  Jones, which are comparable to the reported high-performance

Pb-based perovskite PDs and higher than those of the Pb-free perovskite PDs [35–44]; the detailed comparison is shown in Table S2. The achievement of the high performance is due to the dual passivation of perovskite defects through the BMIMCl and the PMMA, which greatly reduce the dark current, thereby reduce the device noise level and improve the detection capability of the device. Moreover, the broad light absorption range of the CsSnI<sub>3</sub> enables the wide work region of our PD ranging from ultraviolet to infrared radiation, as shown in Fig. S5b. Furthermore, our device shows the  $f_{-3\text{dB}}$  bandwidth of 1196 Hz (Fig. 4e) and the rise/fall time ( $\tau_{rise}/\tau_{fall}$ ) of 0.23/0.19 ms (Fig. 4f).

Device stability is a key parameter of the PD, which is an important reference for commercialization. To confirm the improvement in device stability by the dual passivation strategies, we perform the stability of the unpackaged PDs under different conditions in air (25 °C, 50% humidity), as shown in Fig. 5. We find the performance of the passivated device shows no degradation when it is exposed to continuous light in air for more than 1200 s, but the light current of the original device indicates a significantly decline (Fig. 5a). We further place the devices in air for more than 60 days, and the performance of the original CsSnI<sub>3</sub> PDs decreases to about 30% of the initial value. However, the device performance of the passivated devices remains 90% of the initial value after the same storage time. These results demonstrate

that the introduction of the BMIMCl and PMMA not only enhances the optoelectronic performance of the device, but also improves the stability of the device.

## 4 Conclusions

In conclusion, the BMIMCl was introduced in CsSnI<sub>3</sub> NWs to passivate the Sn vacancies and reduce the dark current of the CsSnI<sub>3</sub> NWPDs. Experimental analysis and theoretical calculation demonstrate that BMIM<sup>+</sup> ions can effectively suppress the oxidation of Sn<sup>2+</sup> to Sn<sup>4+</sup> in the BMIMCl+CsSnI<sub>3</sub> sample. For further reduce the dark current of the devices, the PMMA was applied, and finally, the dual passivated CsSnI<sub>3</sub> NW PDs show ultra-high performance with an ultra-low dark current of  $2 \times 10^{-11}$  A, a responsivity of up to 0.237 A W<sup>-1</sup>, a high detectivity of  $1.18 \times 10^{12}$  Jones and a linear dynamic range of 180 dB. Furthermore, our unpackaged devices exhibit ultra-high stability in device performance after 60 days of storage in air (25 °C, 50% humidity), with the device performance remaining above 90%. This work provides a simple and effective method for the preparation of high-performance, highly stable Pb-free perovskite photoelectric devices.

**Acknowledgements** We acknowledge grants from the National Natural Science Foundation of China (Nos. 51972101, 62074117, 12134010) and the Shenzhen Fundamental Research Program (No. JCYJ20190808152609307).

**Funding** Open access funding provided by Shanghai Jiao Tong University.

**Open Access** This article is licensed under a Creative Commons Attribution 4.0 International License, which permits use, sharing, adaptation, distribution and reproduction in any medium or format, as long as you give appropriate credit to the original author(s) and the source, provide a link to the Creative Commons licence, and indicate if changes were made. The images or other third party material in this article are included in the article's Creative Commons licence, unless indicated otherwise in a credit line to the material. If material is not included in the article's Creative Commons licence and your intended use is not permitted by statutory regulation or exceeds the permitted use, you will need to obtain permission directly from the copyright holder. To view a copy of this licence, visit <http://creativecommons.org/licenses/by/4.0/>.

**Supplementary Information** The online version contains supplementary material available at <https://doi.org/10.1007/s40820-022-00964-9>.

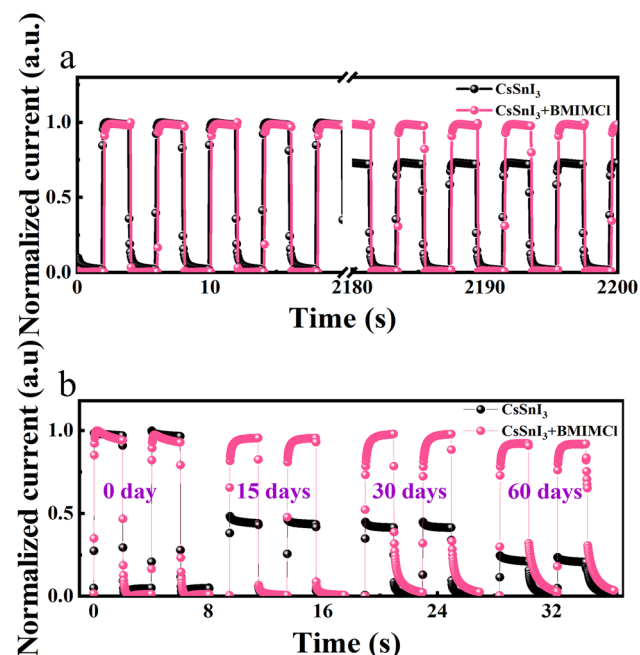


**Fig. 5** Stability of the PD under different conditions in air (25 °C, 50% humidity): **a** stability for long-time testing; **b** stability in long-term storage

## References

1. P. Guo, H. Zhu, W. Zhao, C. Liu, L. Zhu et al., Interfacial embedding of laser-manufactured fluorinated gold clusters enabling stable perovskite solar cells with efficiency over 24%. *Adv. Mater.* **33**(36), 2101590 (2021). <https://doi.org/10.1002/adma.202101590>
2. Y. Zhang, Y. Ma, Y. Wang, X. Zhang, C. Zuo et al., Lead-free perovskite photodetectors: progress, challenges, and opportunities. *Adv. Mater.* **33**(26), 2006691 (2021). <https://doi.org/10.1002/adma.202006691>
3. B.B. Yu, Z. Chen, Y. Zhu, Y. Wang, B. Han et al., Heterogeneous 2D/3D tin-halides perovskite solar cells with certified conversion efficiency breaking 14%. *Adv. Mater.* **33**(36), 2102055 (2021). <https://doi.org/10.1002/adma.202102055>
4. C. Li, Y. Ma, Y. Xiao, L. Shen, L. Ding, Advances in perovskite photodetectors. *InfoMat* **2**(6), 1247–1256 (2020). <https://doi.org/10.1002/inf2.12141>
5. N. Ma, J. Jiang, Y. Zhao, L. He, Y. Ma et al., Stable and sensitive tin-lead perovskite photodetectors enabled by azobenzene derivative for near-infrared acousto-optic conversion communications. *Nano Energy* **86**, 21106113 (2021). <https://doi.org/10.1016/j.nanoen.2021.106113>
6. Z. Shuang, H. Zhou, D. Wu, X. Zhang, B. Xiao et al., Low-temperature process for self-powered lead-free Cs<sub>2</sub>AgBiBr<sub>6</sub> perovskite photodetector with high detectivity. *Chem. Eng.*



- J. **433**, 22134544 (2022). <https://doi.org/10.1016/j.cej.2022.134544>
7. L. Zhang, X. Pan, L. Liu, L. Ding, Star perovskite materials. *J. Semiconduct.* **43**(3), 030203 (2022). <https://doi.org/10.1088/1674-4926/43/3/030203>
  8. X. Tang, H. Zhou, X. Pan, R. Liu, D. Wu et al., All-inorganic halide perovskite alloy nanowire network photodetectors with high performance. *ACS Appl. Mater. Interfaces* **12**(4), 4843–4848 (2020). <https://doi.org/10.1021/acsami.9b21666>
  9. Z. Chu, Q. Ye, Y. Zhao, F. Ma, Z. Yin et al., Perovskite light-emitting diodes with external quantum efficiency exceeding 22% via small-molecule passivation. *Adv. Mater.* **33**(18), 2007169 (2020). <https://doi.org/10.1002/adma.202007169>
  10. H. Min, D.Y. Lee, J. Kim, G. Kim, K.S. Lee et al., Perovskite solar cells with atomically coherent interlayers on SnO<sub>2</sub> electrodes. *Nature* **598**(7881), 444–450 (2021). <https://doi.org/10.1038/s41586-021-03964-8>
  11. X. Pan, J. Zhang, H. Zhou, R. Liu, D. Wu et al., Single-layer ZnO hollow hemispheres enable high-performance self-powered perovskite photodetector for optical communication. *Nano-Micro Lett.* **13**, 70 (2021). <https://doi.org/10.1007/s40820-021-00596-5>
  12. J.J. Yoo, G. Seo, M.R. Chua, T.G. Park, Y. Lu et al., Efficient perovskite solar cells via improved carrier management. *Nature* **590**(7847), 587–593 (2021). <https://doi.org/10.1038/s41586-021-03285-w>
  13. Z. Liu, W. Qiu, X. Peng, G. Sun, X. Liu et al., Perovskite light-emitting diodes with EQE exceeding 28% through a synergetic dual-additive strategy for defect passivation and nanostructure regulation. *Adv. Mater.* **33**(43), 2103268 (2021). <https://doi.org/10.1002/adma.202103268>
  14. T. Ye, K. Wang, Y. Hou, D. Yang, N. Smith et al., Ambient-air-stable lead-free CsSnI<sub>3</sub> solar cells with greater than 7.5% efficiency. *J. Am. Chem. Soc.* **143**(11), 4319–4328 (2021). <https://doi.org/10.1021/jacs.0c13069>
  15. N.K. Tailor, P. Maity, S. Satapathi, Observation of negative photoconductivity in lead-free Cs<sub>3</sub>Bi<sub>2</sub>Br<sub>9</sub> perovskite single crystal. *ACS Photon.* **8**(8), 2473–2480 (2021). <https://doi.org/10.1021/acsphotonics.1c00702>
  16. L.J. Chen, Synthesis and optical properties of lead-free cesium germanium halide perovskite quantum rods. *RSC Adv.* **8**(33), 18396–18399 (2018). <https://doi.org/10.1039/c8ra01150h>
  17. A. Singh, P.T. Lai, A. Mohapatra, C.Y. Chen, H.W. Lin et al., Panchromatic heterojunction solar cells for Pb-free all-inorganic antimony based perovskite. *Chem. Eng. J.* **419**, 21129424 (2021). <https://doi.org/10.1016/j.cej.2021.129424>
  18. C. Pareja-Rivera, D. Solis-Ibarra, Reversible and irreversible thermochromism in copper-based halide perovskites. *Adv. Opt. Mater.* **9**(15), 2100633 (2021). <https://doi.org/10.1002/adom.202100633>
  19. H.H. Fang, S. Adjokatsé, S. Shao, J. Even, M.A. Loi, Long-lived hot-carrier light emission and large blue shift in formamidinium tin triiodide perovskites. *Nat. Commun.* **9**, 243 (2018). <https://doi.org/10.1038/s41467-017-02684-w>
  20. M.A. Kamarudin, D. Hirotani, Z. Wang, K. Hamada, K. Nishimura et al., Suppression of charge carrier recombination in lead-free tin halide perovskite via lewis base post-treatment. *J. Phys. Chem. Lett.* **10**(17), 5277–5283 (2019). <https://doi.org/10.1021/acs.jpcclett.9b02024>
  21. I. Chung, B. Lee, J. He, R.P. Chang, M.G. Kanatzidis, All-solid-state dye-sensitized solar cells with high efficiency. *Nature* **485**(7399), 486–489 (2012). <https://doi.org/10.1038/nature11067>
  22. K. Marshall, M. Walker, R. Walton, R. Hatton, Enhanced stability and efficiency in hole-transport-layer-free CsSnI<sub>3</sub> perovskite photovoltaics. *Nat. Energy* **1**, 16178 (2016). <https://doi.org/10.1038/nenergy.2016.178>
  23. T. Ye, L. Pan, Y. Yang, Q. Liang, Y. Lu et al., Synthesis of highly-oriented black CsPbI<sub>3</sub> microstructures for high-performance solar cells. *Chem. Mater.* **32**(7), 3235–3244 (2020). <https://doi.org/10.1021/acs.chemmater.0c00427>
  24. J. Chen, Z. Luo, Y. Fu, X. Wang, K.J. Czech et al., Tin(IV)-tolerant vapor-phase growth and photophysical properties of aligned cesium tin halide perovskite (CsSnX<sub>3</sub>, X = Br, I) nanowires. *ACS Energy Lett.* **4**(5), 1045–1052 (2019). <https://doi.org/10.1021/acsenergylett.9b00543>
  25. M. Han, J. Sun, M. Peng, N. Han, Z. Chen et al., Controllable growth of lead-free all-inorganic perovskite nanowire array with fast and stable near-infrared photodetection. *J. Phys. Chem. C* **123**(28), 17566–17573 (2019). <https://doi.org/10.1021/acs.jpcc.9b03289>
  26. M. Konstantakou, T. Stergiopoulos, A critical review on tin halide perovskite solar cells. *J. Mater. Chem. A* **5**(23), 11518–11549 (2017). <https://doi.org/10.1039/c7ta00929a>
  27. M. Lai, Q. Kong, C.G. Bischak, Y. Yu, L. Dou et al., Structural, optical, and electrical properties of phase-controlled cesium lead iodide nanowires. *Nano Res.* **10**(4), 1107–1114 (2017). <https://doi.org/10.1007/s12274-016-1415-0>
  28. Y. Zhou, J. Luo, Y. Zhao, C. Ge, C. Wang et al., Flexible linearly polarized photodetectors based on all-inorganic perovskite CsPbI<sub>3</sub> nanowires. *Adv. Opt. Mater.* **6**(22), 1800679 (2018). <https://doi.org/10.1002/adom.201800679>
  29. M. Li, W.W. Zuo, Y.G. Yang, M.H. Aldamasy, Q. Wang et al., Tin halide perovskite films made of highly oriented 2D crystals enable more efficient and stable lead-free perovskite solar cells. *ACS Energy Lett.* **5**(6), 1923–1929 (2020). <https://doi.org/10.1021/acsenergylett.0c00782>
  30. T. Ye, B. Zhou, F. Zhan, F. Yuan, S. Ramakrishna et al., Below 200 °C fabrication strategy of black-phase CsPbI<sub>3</sub> film for ambient-air-stable solar cells. *Solar RRL* **4**(5), 2000014 (2020). <https://doi.org/10.1002/solr.202000014>
  31. T. Ye, A. Bruno, G. Han, T.M. Koh, J. Li et al., Efficient and ambient-air-stable solar cell with highly oriented 2D@3D perovskites. *Adv. Funct. Mater.* **28**(30), 1801654 (2018). <https://doi.org/10.1002/adfm.201801654>
  32. X. Zheng, Y. Hou, C. Bao, J. Yin, F. Yuan et al., Managing grains and interfaces via ligand anchoring enables 22.3%-efficiency inverted perovskite solar cells. *Nat. Energy* **5**(2), 131–140 (2020). <https://doi.org/10.1038/s41560-019-0538-4>



33. H. Zhou, Z. Song, C.R. Grice, C. Chen, J. Zhang et al., Self-powered CsPbBr<sub>3</sub> nanowire photodetector with a vertical structure. *Nano Energy* **53**, 880–886 (2018). <https://doi.org/10.1016/j.nanoen.2018.09.040>
34. J. Zeng, C. Meng, X. Li, Y. Wu, S. Liu, H. Zhou, H. Wang, H. Zeng, Interfacial-tunneling-effect-enhanced CsPbBr<sub>3</sub> photodetectors featuring high detectivity and stability. *Adv. Funct. Mater.* **29**(51), 1904461 (2019). <https://doi.org/10.1002/adfm.201904461>
35. C. Bao, J. Yang, S. Bai, W. Xu, Z. Yan et al., High performance and stable all-inorganic metal halide perovskite-based photodetectors for optical communication applications. *Adv. Mater.* **30**(38), 1803422 (2018). <https://doi.org/10.1002/adma.201803422>
36. J. Li, G. Zhang, Z. Zhang, J. Li, Z. Uddin et al., Defect passivation via additive engineering to improve photodetection performance in CsPbI<sub>2</sub>Br perovskite photodetectors. *ACS Appl. Mater. Interfaces* **13**(47), 56358–56365 (2021). <https://doi.org/10.1021/acscami.1c19323>
37. X. Li, D. Yu, F. Cao, Y. Gu, Y. Wei et al., Healing all-inorganic perovskite films via recyclable dissolution–recrystallization for compact and smooth carrier channels of optoelectronic devices with high stability. *Adv. Funct. Mater.* **26**(32), 5903–5912 (2016). <https://doi.org/10.1002/adfm.201601571>
38. Z. Li, X. Liu, C. Zuo, W. Yang, X. Fang, Supersaturation-controlled growth of monolithically integrated lead-free halide perovskite single-crystalline thin film for high-sensitivity photodetectors. *Adv. Mater.* **33**(41), 2103010 (2021). <https://doi.org/10.1002/adma.202103010>
39. S.K. Shil, F. Wang, Z. Lai, Y. Meng, Y. Wang et al., Crystalline all-inorganic lead-free Cs<sub>3</sub>Sb<sub>2</sub>I<sub>9</sub> perovskite microplates with ultra-fast photoconductive response and robust thermal stability. *Nano Res.* **14**(11), 4116–4124 (2021). <https://doi.org/10.1007/s12274-021-3351-x>
40. A. Waleed, M.M. Tavakoli, L. Gu, Z. Wang, D. Zhang et al., Lead-free perovskite nanowire array photodetectors with drastically improved stability in nanoengineering templates. *Nano Lett.* **17**(1), 523–530 (2017). <https://doi.org/10.1021/acs.nanolett.6b04587>
41. J. Wang, S. Xiao, W. Qian, K. Zhang, J. Yu et al., Self-driven perovskite narrowband photodetectors with tunable spectral responses. *Adv. Mater.* **33**(3), 2005557 (2021). <https://doi.org/10.1002/adma.202005557>
42. X. Wu, J. Sun, H. Shao, Y. Zhai, L. Li et al., Self-powered UV photodetectors based on CsPbCl<sub>3</sub> nanowires enabled by the synergistic effect of acetate and lanthanide ion passivation. *Chem. Eng. J.* **426**, 131310 (2021). <https://doi.org/10.1016/j.cej.2021.131310>
43. X. Xu, C. Fan, Z. Qi, S. Jiang, Q. Xiao et al., CsCu<sub>2</sub>I<sub>3</sub> nanoribbons on various substrates for UV photodetectors. *ACS Appl. Nano Mater.* **4**(9), 9625–9634 (2021). <https://doi.org/10.1021/acsnanm.1c02041>
44. F. Zhu, G. Lian, B. Yu, T. Zhang, L. Zhang et al., Pressure-enhanced vertical orientation and compositional control of ruddlesden–popper perovskites for efficient and stable solar cells and self-powered photodetectors. *ACS Appl. Mater. Interfaces* **14**(1), 1526–1536 (2021). <https://doi.org/10.1021/acscami.1c18522>